**Structural Engineering and Mechanics**, *Vol. 70, No. 6 (2019) 723-735*
DOI: https://doi.org/10.12989/sem.2019.70.6.723


# Experimental and numerical investigation of track-bridge interaction for a long-span bridge

Ji Zhang[1,2a], Dingjun Wu[2b], Qi Li[*2] and Yu Zhang[3c]

*[1]School of Civil Engineering, Suzhou University of Science and Technology, 1701 Binhe Road, Suzhou, Jiangsu 215011, China*
*[2]Department of Bridge Engineering, Tongji University, 1239 Siping Road, Shanghai 200092, China*
*[3]Department of Civil & Environmental Engineering, University of California, Los Angeles, CA 90095, USA*

*(Received June 11, 2018, Revised March 18, 2019, Accepted March 19, 2019)*

**Abstract.** Track-bridge interaction (TBI) problem often arises from the adoption of modern continuously welded rails. Rail expansion devices (REDs) are generally required to release the intensive interaction between long-span bridges and tracks. In their necessity evaluations, the key techniques are the numerical models and methods for obtaining TBI responses. This paper thus aims to propose a preferable model and the associated procedure for TBI analysis to facilitate the designs of long-span bridges as well as the track structures. A novel friction-spring model was first developed to represent the longitudinal resistance features of fasteners with or without vertical wheel loadings, based on resistance experiments for three types of rail fasteners. This model was then utilized in the loading-history-based TBI analysis for an urban rail transit dwarf tower cable-stayed bridge installed with a RED at the middle. The finite element model of the long-span bridge for TBI analysis was established and updated by the bridge's measured natural frequencies. The additional rail stresses calculated from the TBI model under train loadings were compared with the measured ones. Overall agreements were observed between the measured and the computed results, showing that the proposed TBI model and analysis procedure can be used in further study.

**Keywords:** track-bridge interaction; continuously welded rail; fastener resistance; loading-history; rail expansion device; field test; cable-stayed bridge

## 1. Introduction

The technology of continuous welded rail (CWR) has been widely adopted in modern railway system to reduce the maintenance of the track structures and to enhance the ride quality of the trains (Lim *et al.* 2003). With larger expansion lengths, track-bridge interaction (TBI) problems are more likely to arise on long-span bridges with CWRs, which can lead to breaking or buckling of the rails (Esveld 2001, Okelo and Olabimtan 2011). Although rail expansion devices (REDs) can effectively release the intensive interaction between long-span bridges and tracks subjected to temperature loading and braking/accelerating of the trains, they bring additional construction and maintenance costs in the tracks, and jeopardize the running comfort and safety of the trains (Esveld 1995, Dai and Liu 2013). Thus, it is wise to avoid the use of these devices unless other measures don't work in practice. In the decision-making of whether such devices must be installed on a given bridge, the crucial techniques are the numerical methods and models that can obtain true TBI responses with better accuracy.

The topic of TBI problem is not new in railway science and engineering (Wenner *et al.* 2016) but has regained lots of focuses recently in China, Indian and other countries to meet the rapid development in rail traffic (Hu *et al.* 2014, Mirza *et al.* 2016). Previous works mainly focused on commonly-used simply supported bridges (Ruge and Birk 2007, Ruge *et al.* 2009, Okelo and Olabimtan 2011, Zhang *et al.* 2015) and continuous bridges (Bin *et al.* 2012, Dai and Liu 2013) with small-to-medium spans. Nowadays, more long-span bridges including arch bridges and cable-stayed bridges are being constructed on rail transit lines to adapt to the complex terrain and high navigation clearance (Gimsing and Georgakis 2011, Chen *et al.* 2013). This makes the TBI analyses for long-span bridges increasingly important, not only for the more intensive TBI responses led by larger spans, but also due to the increasing demand towards the optimization of REDs through more accurate TBI analysis (Liu *et al.* 2013). Therefore, the appropriate locations of REDs, and the alternative schemes, such as the optimized longitudinal restraint conditions (Dai and Yan 2012, Liu *et al.* 2013), small or zero resistance fasteners (Esveld 1995) were investigated with regard to their efficiencies in mitigating TBI responses. Computing programs (Chen *et al.* 2013) and simplified algorithms (Wang *et al.* 2013) were also developed to facilitate the TBI analysis for long-span bridges.

The above investigations on long-span bridge-track interaction have extended the research on this field, yet

*Corresponding author, Associate Professor
E-mail: liqi_bridge@tongji.edu.cn
[a] Ph.D.
E-mail: 071190@tongji.edu.cn
[b] Professor
E-mail: tjwdj@tongji.edu.cn
[c] Ph.D. student
E-mail: y.zhang@ucla.edu


http://www.techno-press.com/journals/sem&subpage=7
ISSN: 1225-4568 (Print), 1598-6217 (Online)

these studies all followed the conventional linear superposition method for different load cases, as recommended by German code DIN-Fb 101 (2003), Eurocode EN 1991-2 (2003), UIC recommendation 774-3R (2001), Spanish IAPF (2007), Chinese high speed railway (HSR) code TB 10621-2009 (2009), and Chinese CWR code TB 10015-2012 (2012). Despite the use of the elastic-plastic resistance model, the linear superposition method still disobeys the nonlinear nature of the TBI, and might overestimate or underestimate the TBI responses due to the neglecting of loading-history effects, as illustrated by Ruge and Birk (2007), Widarda (2008), Zhang et al. (2015), and Yang and Jang (2016) in the TBI analysis for bridges with regular spans. For bridges with longer spans, the nonlinear combination of loading effects could bring more considerable reduction in rail stresses (Ruge and Birk 2007). As a result, REDs may not be required for certain long-span bridges if reasonable TBI responses could be obtained through more accurate analysis.

The fastener resistance models have significant effect on the TBI responses of long-span bridges (Dai and Liu 2013, Liu *et al.* 2013). In order to facilitate an accurate numerical simulation, laboratory and/or field measurements are therefore required to determine the longitudinal resistance properties of fasteners in specific conditions (Esveld 1998). For example, field measurements on Altmühl bridge with ballasted track showed that the unloaded longitudinal stiffness of the coupling system consisting of rail pads and ballast were 3.45 times larger than the one recommended by EN 1991-2 (2003) due to possible glued ballast (Widarda 2008). Ryjáček and Vokáč (2014) conducted a long-term monitoring of the track-bridge system under thermal variation on a bridge with an unusual combination of ballasted track, direct fastening and a barrier in the ballast. New resistance models defining the connections between the rail and the bridge were introduced and verified based on the measured data. A small-scale laboratory test was performed by Ryjáček *et al.* (2016) to determine the longitudinal resistance model of the Embedded Rail System under various vertical loads. Longitudinal resistance tests during unloading conditions and the transformation between the unloaded and loaded conditions in the vertical direction are crucial in establishing the longitudinal track stiffness laws that comply with the load history concept, as was done by Yang and Jang (2016). Various field tests were also performed to ensure that the finite element (FE) models could predict the realistic interaction behaviors within acceptable error margin (UIC 774-3R 2001, Mirza *et al.* 2016, Backer *et al.* 2017).

Zhang *et al*. (2015) proposed a loading-history method for TBI analysis with the so-called double-spring model to simulate the behavior of the fasteners before and after the train enters the bridge. This study aims to extend our latest research from commonly-used simple bridges to a long-span cable-stayed bridge, using similar loading-history framework but a novel fastener model. A series of laboratory tests were conducted on three types of rail fasteners frequently used in urban rail transit traffic in China, with emphasis on the transforming of resistance displacement curves (RDCs) between a vertically unloaded situation and a loaded situation. A friction-spring model was proposed to describe the nonlinear resistance features of the fasteners and to convey more explicit physical meanings than the previous double-spring model. Field tests were also conducted on a cable-stayed bridge on the urban rail transit line in Shanghai to obtain the free vibration characteristic of the bridge and the longitudinal rail stresses under train loadings. TBI model of this bridge was then established using the experimental fastener resistance and the updated foundation stiffness of the bridge. The additional rail stresses under various loading conditions were calculated and then compared with the measured ones.

## 2. Fastener resistance model for loading-history-based TBI analysis

By using the testing facility (see Fig. 1(a)) that could exert vertical and longitudinal forces on the test rail and simultaneously measure the longitudinal displacements of the rail, Zhang *et al*. (2015) have conducted laboratory tests to determine the RDCs of a WJ-2 fastener shown in Fig. 1(b). A double-spring model from the experimental results was directly adopted to represent the RDCs of the fastener with and without vertical loadings. This model was true to the experimental results but it lacked mechanical meanings because no physical parameter of the fastener was involved in the model. In order to generalize a resistance model based on the mechanical analysis of the fastening system, the facility mentioned above was again employed to obtain the nonlinear features of two more fasteners widely used on the urban rail transit traffic in China, i.e., the DTIII-2 type small resistance fastener (see Fig. 1(c)) and the Cologne-Egg-like vibration damping fastener (Fig. 1(d)). A total of 247 times of resistance tests were conducted for three types of fasteners (131 times for the WJ-2 fastener, 64 times for the DTIII-2 fastener, and 52 times for the Cologne-Egg-like fastener) for statistical analysis. Four clamping forces of the clips measured in field were taken into account by loosening or over-screwing the T-bolts of the fasteners to check their effects on the resistance of the fastening system. The clamping forces were transformed into equivalent torsional moments, and were applied and controlled by the preset torque wrench. These tests not only considered the effect of the vertical loadings, but also the transition from the vertically unloaded condition to the loaded condition and that in the reverse order.

### *2.1 Friction-spring model for the fastener resistance*

Fig. 2(a) illustrates a concrete model of a fastener to assist the understanding on the nature of resistance force. The abstract friction-spring model was also depicted in Fig. 2(b), in which one linear spring and two friction springs were used respectively to simulate the elastic deformation of the fastener and the possible sliding in the rail against the fastener. The longitudinal elastic stiffness $k$ of the fastener, provided by the rail-pad and the clips, enables the initial longitudinal motion of the rail relative to the roadbed before the overcome of the maximum static friction force on the upper and lower surfaces of the bottom flange of the rail. The elastic stiffness $k$ was assumed to remain unchanged

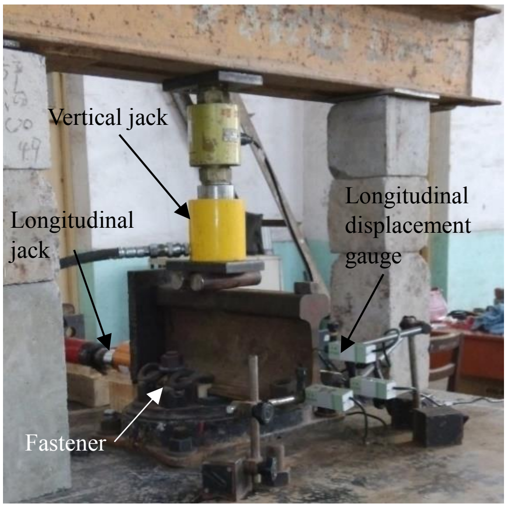


(a) testing facility

(b) WJ-2 fastener

(c) DTIII-2 fastener

(d) Cologne-Egg-like fastener

Fig. 1 Testing facility and three types of fasteners for test

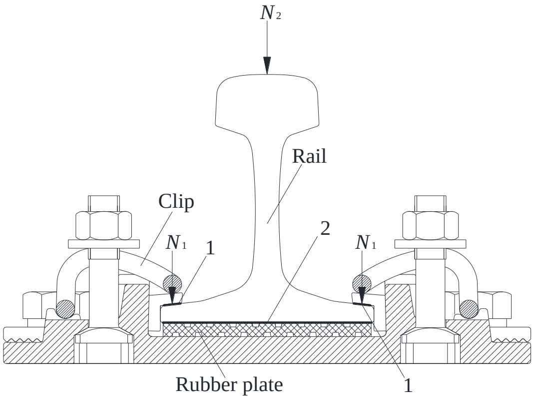


(a) concrete model of a fastener

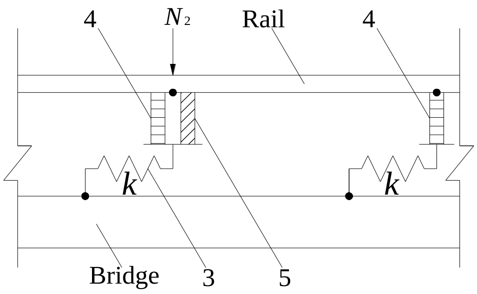


(b) abstract friction–spring model

1. Contact surface between the rail and the clip, with the friction coefficient of $\mu_1$; 2. Contact surface between the rail and the rubber plate, with the friction coefficient of $\mu_2$; 3. Linear spring modelling the stiffness of the fastener; 4. Friction spring I modelling the maximum static friction when unloaded; 5. Friction spring II modelling the increase in the maximum static friction induced by vertical load, activated when train arrives at the bridge; $N_1$. Clamping force; $N_2$: Static wheel load born by one fastener.

Fig. 2 The friction–spring model of a fastener

with or without vertical load. The longitudinal stiffness values of the loaded and unloaded track were quite close to each other according to the experiment conducted on the Embedded Rail fastening System (Ryjáček *et al.* 2016). Measurement data will also be used to substantiate this assumption later.

When the rail is vertically unloaded in the initial analysis of temperature effects, the maximum static friction force $F_u$ can be obtained as

$$F_u=2(\mu_1+\mu_2)N_1 \tag{1}$$

where $\mu_1$ and $\mu_2$ are the friction coefficients of the upper and lower surfaces respectively; $N_1$ denotes the compression force on the upper and lower surfaces of the rail flange induced by a clip, which is approximately proportional to the torsional moment of the T-bolts; and the factor of 2 represents two clips within one fastener. In the abstract

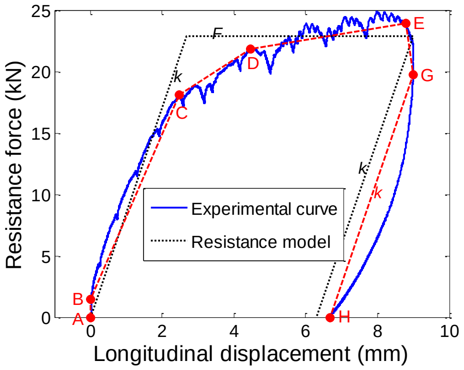


Fig. 3 Typical data processing procedure

model, the nonlinear behaviour of each fastener without the vertical load is embodied by the linear spring (with the stiffness coefficient of $k$) in series with the friction spring I (with the maximum static friction force of $F_u$).

When the rail is vertically loaded with the arrival of trains, the maximum static friction force increases as the additional compression force $N_2$ is exerted on the contact surface between the rail and the rail pad. Since the WJ-2 and DTIII-2 fastener are both equipped with hard rubber plates, the vertical stiffness of these two fasteners (40 kN/mm for the WJ-2 fastener, 25 kN/mm for the DTIII-2 fastener) are reckoned to be large enough that the loss of the clamping force $N_1$ while applying the wheel load $N_2$ could be neglected. Such assumption might lead to some error in the resistance model of the Cologne-Egg-like fastener since more flexible rubber plate is installed to mitigate the vibration.

Different from metallic contact, laboratory-controlled investigations show that the coefficient of rubber friction ($\mu$) drops as the normal pressure ($P$) increases, but with a gradually decreasing slope (Roth *et al.* 1943, Smith 2008). Roth *et al.* (1943) conducted investigations on rubber friction over glass track, a gentle downslope of the P-$\mu$ curve was observed when reaching the maximum pressure of $2.76\times10^5$ Pa. Deladi (2006) studied the multi-asperity static friction in rubber-metal contact, and similar trend was found: such decreasing effect could be neglected when the vertical pressure in the rubber is larger than $3.33\times10^4$ Pa. As for the fasteners tested in this study, the rubber pressure induced solely by the clamping force has reached $3.14\times10^5$ Pa, indicating that the coefficient of friction between the rail and the rubber plate has already entered a relatively stable zone. Hence $\mu_2$ was assumed to maintain a constant state despite the exertion of $N_2$. Based on these assumptions, the maximum static friction force $F_l$ between the rail and the fastener when vertically loaded can be expressed as

$$F_l=2(\mu_1+\mu_2)N_1+\mu_2N_2 \tag{2}$$

The friction spring II with the maximum static friction of $\mu_2N_2$ should be activated in parallel to the friction spring I (see Fig. 2(b)) in the abstract model accordingly. Likewise, the friction spring II should be deactivated with the leaving of the train.

From the above discussion, one may notice the convenience of the friction-spring model for connecting the longitudinal resistance of rail fasteners with vertical load conditions using friction coefficients. Thus this model will facilitate the loading-history-based TBI analysis similar to the double-spring model proposed by Zhang *et al.* (2015). Compared with the double-spring model by using specific RDCs without explicit physical meanings, the friction-spring model gives a uniform definition of the longitudinal resistance in various load cases. Moreover, this model could be more easily established in the TBI model using the FE method once the three mechanical parameters $k$, $\mu_1$ and $\mu_2$ of a certain fastener were determined by laboratory tests.

### *2.2 Determination of the model parameters from experimental results*

After going through all the RDCs of the fastener from test, a typical experimental curve of the vertically loaded case is illustrated in Fig. 3, together with 7 characteristic points from A to H extracted from the curve. The fastener shall experience pseudo-elastic deformation from point A to C under small longitudinal jack force on the rail, elasto-plastic hardening from point C to D with the increasing of the force, plastic sliding from point D to E when the external force overcomes the friction force, and elastic recovery from points E to H as the jack force is unloaded. The vertically unloaded curves showed similar trend, thus treatment should follow the same concept described above.

To obtain the key mechanical parameters of the fastening system, the measured data were manifested in the following way. First, the average slope of the unloading curve between points G and H, was used to represent the stiffness $k$ of the fastening system. The test results under both vertically unloaded and loaded conditions were included in the statistical analysis of the spring stiffness $k$.

One can notice that the pseudo-elastic displacement during loading is significantly larger than the recoverable elastic displacement. This is owing to the possible gaps in the virgin rail-fastener system, which could be eliminated by exerting cyclic loadings (Zhang *et al.* 2015). The sharp curve from point E to G was also ruled out for the determination of stiffness $k$ because it might be caused by hysteresis effect of the testing facility subjected to sharp changes in the longitudinal jack force.

Second, the average resistance forces at point D and E under vertically unloaded and loaded situations could well represent the maximum static friction forces $F_u$ and $F_l$ respectively, which could be then applied to derive the friction coefficient $\mu_1$ and $\mu_2$ by using Eqs. (1)-(2)

$$\begin{cases}\mu_1=\dfrac{F_u}{2N_1}-\dfrac{F_l-F_u}{N_2}\\ \mu_2=\dfrac{F_l-F_u}{N_2}\end{cases} \tag{3}$$

According to the fastener brochure, a clamping force of 4 kN can be generated by the T-bolt with the recommended torsional moment of 80 N·m. The clamping forces under other torsional moments were deduced using linear interpolation method. One rail pad-fastener pair bore half of the static wheel load at most in instances where multi-fasteners were located under the rail (Zhang *et al.* 2015).

Table 1 Test parameters of friction–spring model for DTIII-2, WJ-2, and Cologne-Egg-like fasteners

| | Torsional moment (N·m) | | 60 | | 80 | | 100 | | 120 | | AVG* |
|---|---|---|---|---|---|---|---|---|---|---|---|
| WJ-2 | $F$ (kN) | $F_u$ (C.V.*) | 4.87 | (4.7%) | 6.98 | (8.6%) | 7.95 | (8.2%) | 8.72 | (5.8%) | - |
| | | $F_l$ (C.V.) | 21.29 | (2.2%) | 23.18 | (3.4%) | 22.57 | (5.0%) | 24.69 | (5.9%) | - |
| | $k$ (kN/mm) | $k$ (C.V.) | 4.34 | (6.5%) | 5.04 | (12.9%) | 5.32 | (11.8%) | 6.21 | (10.4%) | 6.80 |
| | | | 7.73 | (4.9%) | 8.65 | (4.6%) | 8.27 | (5.3%) | 8.81 | (5.9%) | |
| | $\mu$ | $\mu_1$ | 0.40 | | 0.47 | | 0.43 | | 0.33 | | 0.41 |
| | | $\mu_2$ | 0.41 | | 0.41 | | 0.37 | | 0.40 | | 0.40 |
| DTIII-2 | $F$ (kN) | $F_u$ (C.V.) | - | | 4.11 | (11.4%) | 4.81 | (8.6%) | 5.41 | (9.7%) | - |
| | | $F_l$ (C.V.) | - | | 17.84 | (5.3%) | 18.40 | (6.0%) | - | | - |
| | $k$ (kN/mm) | $k$ (C.V.) | - | | 10.02 | (13.9%) | 10.66 | (5.0%) | 10.46 | (9.6%) | 8.31 |
| | | | - | | 6.63 | (2.5%) | 5.86 | (5.4%) | - | | |
| | $\mu$ | $\mu_1$ | - | | 0.17 | | 0.14 | | - | | 0.16 |
| | | $\mu_2$ | - | | 0.34 | | 0.34 | | - | | 0.34 |
| Cologne-Egg | $F$ (kN) | $F_u$ (C.V.) | - | | 6.13 | (1.9%) | 8.54 | (2.5%) | - | | - |
| | | $F_l$ (C.V.) | - | | 29.57 | (2.3%) | 28.99 | (2.1%) | - | | - |
| | $k$ (kN/mm) | $k$ (C.V.) | - | | 6.84 | (7.2%) | 6.65 | (6.8%) | - | | 7.02 |
| | | | - | | 8.03 | (4.9%) | 6.56 | (3.0%) | - | | |
| | $\mu$ | $\mu_1$ | - | | 0.18 | | 0.34 | | - | | 0.26 |
| | | $\mu_2$ | - | | 0.59 | | 0.51 | | - | | 0.55 |

*C.V.: coefficient of variation; AVG: average value

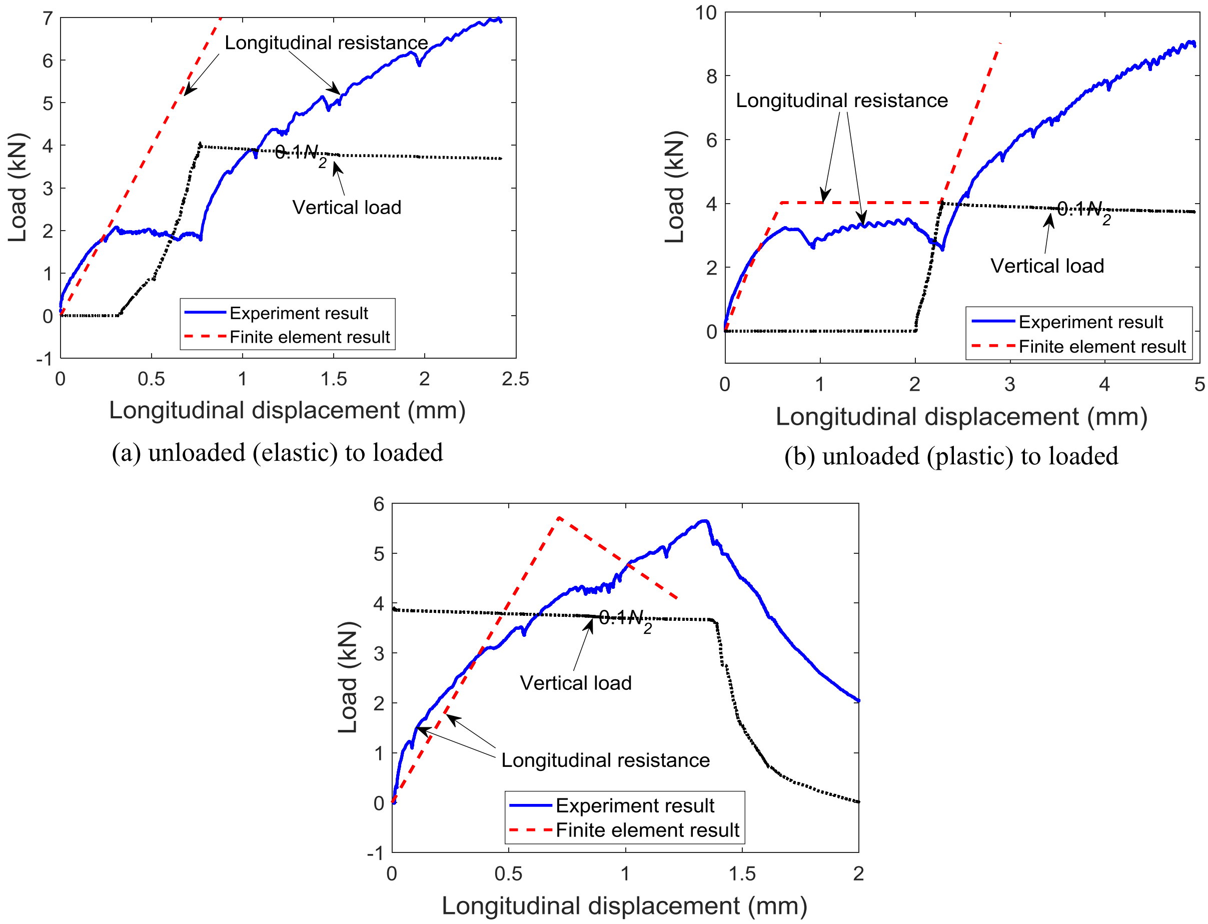


(a) unloaded (elastic) to loaded

(b) unloaded (plastic) to loaded

(c) loaded (elastic) to unloaded

Fig. 4 Comparison of RDC transformation modes of the DTIII-2 fastener

Therefore, $N_2$ was set to be 40 kN in the tests (GB 50157-2013 2014).

Table 1 lists the statistical data of the maximum static friction forces $F_u$ and $F_1$, the spring stiffness $k$ and the friction coefficients $\mu_1$ and $\mu_2$ of the three fastener types under various torsional moments, by using the above data processing method.

These data were convincing in that the coefficients of variation (C.V.s) were generally within 5%, and only a few were around 10%. The fact that the derived mechanical parameters of the fasteners ($k$, $\mu_1$ and $\mu_2$) were quite close to each other under different torsional moments and vertical loading conditions, further substantiates the presenting of the friction-spring model in this study to describe the fastening system through its inherent characteristic parameters. Only the clamping force of 4 kN corresponding to the recommend torsional moment of 80 N·m was used when applying this friction-spring model into FE analysis.

### 2.3 Verification of the resistance model under loading transformations

To further verify the proposed friction-spring model allowing for loading-history analysis, additional tests were conducted on the DTIII-2 fastener to obtain the RDCs during the transformation modes from vertically unloaded to loaded and from loaded to unloaded. A FE model employing the proposed friction-spring model was also established to simulate the testing procedures on a single fastener. And the parameters for the FE model were based on test results of the DTIII-2 fastener where $k$ = 8.31 kN/mm, $\mu_1$ = 0.16, $\mu_2$ = 0.34, $N_1$ = 4 kN, and $N_2$ = 40 kN. Fig. 4 demonstrates the comparisons of the longitudinal RDCs between the experiment and FE results under the following three loading cases. In the meantime, the corresponding vertical loading conditions ($N_2$) were also plotted in Fig. 4.

In the first loading case (see Fig. 4(a)), the vertically unloaded rail moved elastically under the longitudinal force until a vertical load of 40 kN was exerted by hand hydraulic jack and then kept at the same level. A longitudinal displacement of about 0.5 mm was then measured by the displacement gauges due to the disturbance of the vertical load. And the rail continued to move elastically with the increasing of the longitudinal force for some distance along the curve with similar slope before the vertical load was exerted. This testing phenomenon observed from Fig. 4(a) further proved the assumption that the elastic stiffness of the fastener was almost unaffected by the vertical load.

In the second loading case (see Fig. 4(b)), the vertically unloaded rail was pushed longitudinally until it slid against the fastener for more than 1 mm, then a 40 kN vertical load was applied, and the rail regained the ability to move elastically for some distance. With the application of the vertical load, the increase in the maximum friction force allowed the fastener to resist larger resilience force in the rail pad. However, the slope of the FE curve cannot perfectly accord with that of the experimental curve due to the aforementioned initial gaps in the actual coupling system.

In the third loading case (see Fig. 4(c)), the system was initially exerted with vertical load, and the rail moved elastically for some distance until the vertical load was removed suddenly. The resistance force of the fastener decreased at once for the loss in friction force, and the rail was therefore pushed forward until the longitudinal jack force decreased to certain amount that could be resisted by the fastener without vertical loading. As the force-displacement relationship of the longitudinal jack was not perfectly known and the dynamic effect during the motion of the rail was not considered in the FE model, therefore the slope of the computed unloading curve did not match perfectly with the test one.

For these representative loading cases described above, the transformation modes obtained from the proposed friction-spring model generally matched with what the laboratory test exhibited, as illustrated in Fig. 4. Therefore, the proposed friction-spring model can be used in the TBI model to simulate the loading-history effects of the coupled system under transformations between different loading cases.

## 3. Case study

A dwarf-tower cable-stayed bridge (see Figs. 5(a) and (b)) in Shanghai metro line was selected in this study to demonstrate the establishment of the TBI model and the application of the loading-history based analysis. Field tests were conducted on this bridge to obtain the natural vibration characteristics of the bridges and the longitudinal rail stresses under train loadings. The former will be used to update the FE model of the bridge and the latter will be used to validate the TBI model. All the dynamic tests were conducted around midnight in September, when the ambient temperature was about 26 °C. Two metro trains, each with 3 cars, were used in the field tests (see Fig. 5(c)).

The length of the cable-stayed bridge is 300 m with the span arrangement of (80+140+80) m. The main beam is designed as a twin-cell prestressed concrete box girder with a height ranging from 3.0 to 5.6 m. The girder and the pylon are rigidly connected, and the height of the pylon above the deck is designed to be 20.5 m, and its transvers width is 2.5 m. With a total of 2×20 pairs of cables, the longitudinal distance between each cable at the deck level is 5.0 m. Boundary conditions are illustrated in Fig. 5(a). Each side of this cable-stayed bridge is connected to multiple simply-supported bridges with a standard span of 30 m. Small resistance fasteners of type WJ-2 are applied to connect the rails with the rigid roadbed on this long-span bridge as well as the adjacent simply-supported bridges. The fastener span is 0.6 m. REDs (see Fig. 5(d)) are installed at the middle of the cable-stayed bridge according to the conventional TBI analysis carried out by the design institute, for the purpose of reducing excessive additional rail stresses caused by such a long expansion length.

### 3.1 Testing arrangements and results

As the adjacent simply-supported bridges have some influence on the TBI of the cable-stayed bridge

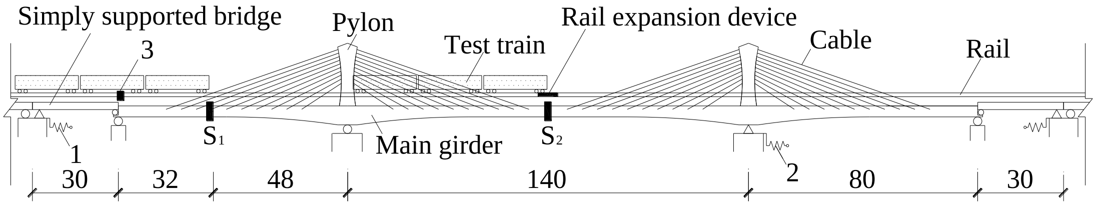


(a) Overall layout (in m)

(b) Site scene

(c) Field test

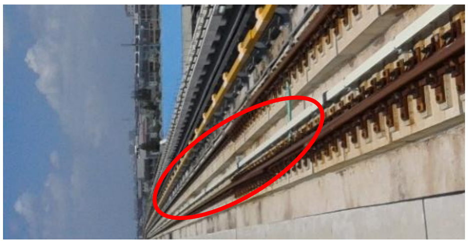

(d) Rail expansion device

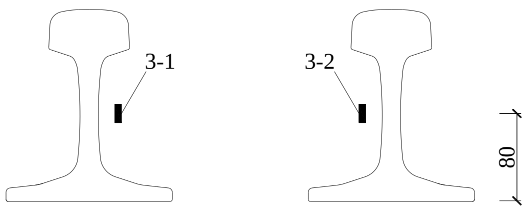


(e) Measuring point of longitudinal rail stress (in mm)

1. Linear spring modelling the piers of simply supported bridge; 2. Linear spring modelling the right main pier of the cable-stayed bridge; 3. Measuring point of longitudinal rail stress; 3-1: Measuring point of longitudinal rail stress on left rail; 3-2: Measuring point of longitudinal rail stress on right rail; $S_1$, $S_2$: Stop location for trains.

Fig. 5 The cable-stayed bridge for field test

(Dai and Yan 2012), acceleration sensors were installed at the mid-span of a simply-supported bridge and the top of its piers to record the vertical and longitudinal responses of the bridge under environmental excitation as well as the testing trains.

The longitudinal fundamental frequency of the beam-pier system ($f_l$) and the vertical fundamental frequency of the system ($f_v$) were identified as 1.80 and 4.60 Hz respectively according to the measured data. Acceleration sensors were also placed on the main girder of the cable-stayed bridge to measure its dynamic responses. Table 2 lists the measured natural frequencies of the first three modes of the cable-stayed bridge in the vertical plan.

The measuring section for longitudinal rail stress (see Fig. 5(a)) was set at the left end of the cable-stayed bridge, at which most severe responses were expected. Strain gauges were placed near the centroids of both rails to minimize the influence of the vertical traffic load (see Fig. 5(e)). Three loading cases were performed in the test: two trains moved towards each other with constant speed and meeting at the middle of the bridge with nonstop; one train stopped at the middle of the side-span (Fig. 5(a), location $S_1$) and then headed towards the right side of the bridge by accelerating; one train stopped at the middle of the main span and accelerated towards the right side of the bridge (Fig. 5(a), location $S_2$). The accelerating rate of the train was set at the stable value of 1.0 m/s$^2$ by the train driver. The test stresses were reset to zero each time before train entering the cable-stayed bridge so that only the vehicle-induced rail stress changes were recorded.

Table 2 The first three natural frequencies of the cable-stayed bridge obtained via field test and the updated finite element model (in Hz)

| Mode Order | Vibration mode | Field test | FE result | Relative deviation* |
|---|---|---|---|---|
| 1 | First-order vertical bending | 0.78 | 0.74 | -4.4% |
| 2 | Second-order vertical bending + First-order longitudinal floating | 1.33 | 1.39 | 5.2% |

*Relative deviation = (FE results- Field test results)/Field test results

Fig. 6 illustrates the measured longitudinal rail stresses with the movement of the vehicle head in the loading case of two trains meeting at the middle of the cable-stayed bridge. Twelve peaks in the rail stress curves representing the dynamic impact of the wheels could be observed at each of the three train speeds. The maximum rail stress zone of the left rail (from point A to point B in Fig. 6) and the right rail (from point C to point D in Fig. 6) were treated as the maximum additional bending stresses of the rail, when two vehicles met at the middle and the deflection of the mid-span reached its maximum value. Table 3 lists the measured additional bending stress of the rail by using the mean value of the maximum rail stress zones of both rails (from point A to B, and point C to D) under three train speeds.

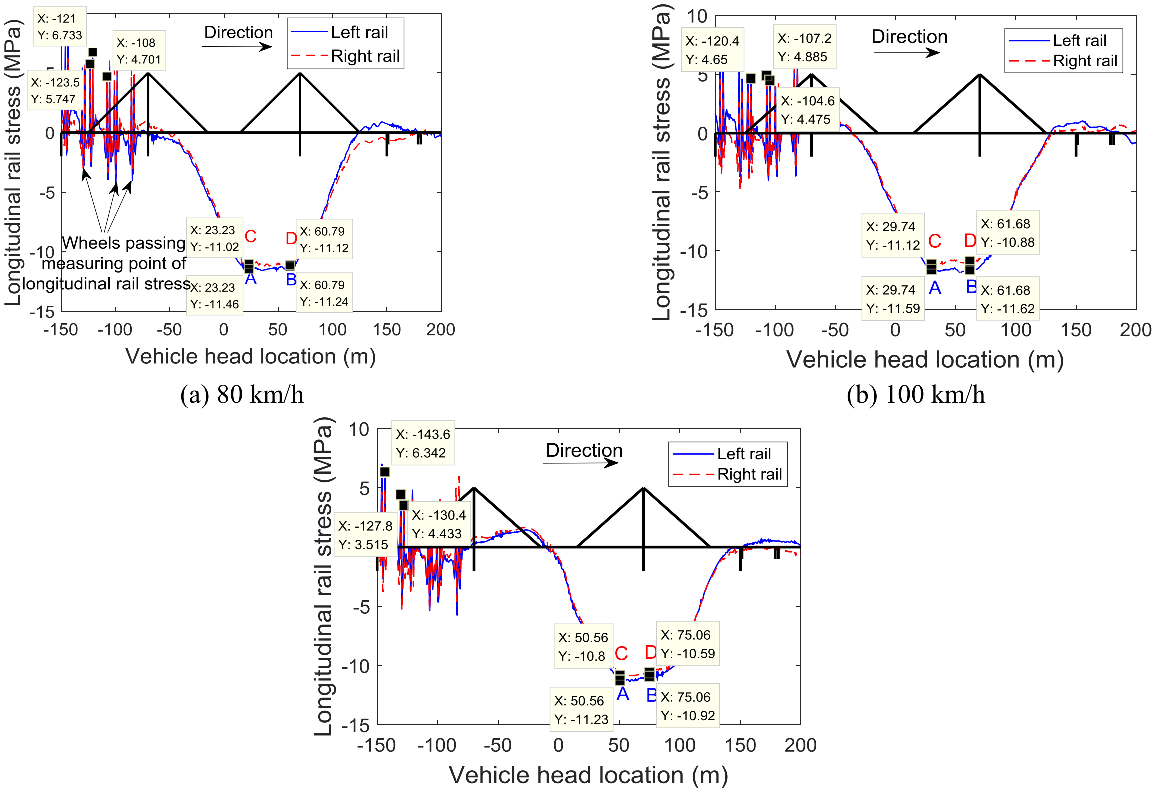

(a) 80 km/h

(b) 100 km/h

(c) 120 km/h

Fig. 6 Measured longitudinal rail stresses at left girder end when trains met at the middle of the cable-stayed bridge

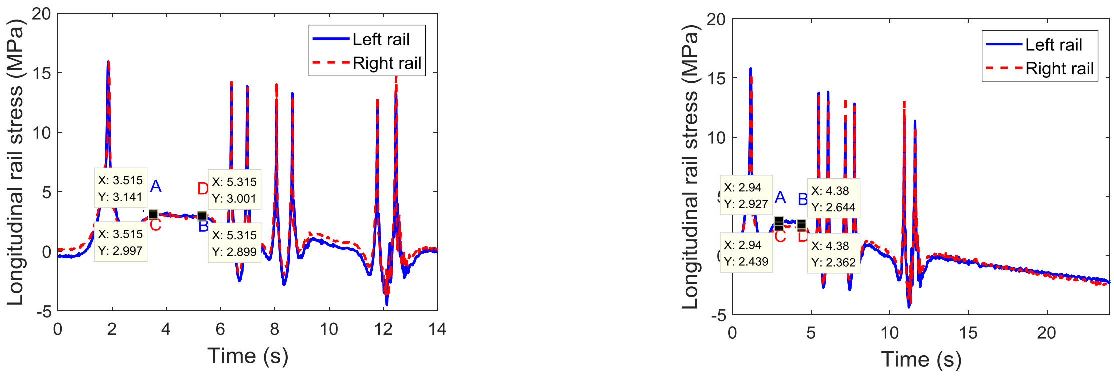

(a) first time

(b) second time

Fig. 7 Measured longitudinal rail stresses at left girder end when one train accelerated at the middle of the side span of the cable-stayed bridge

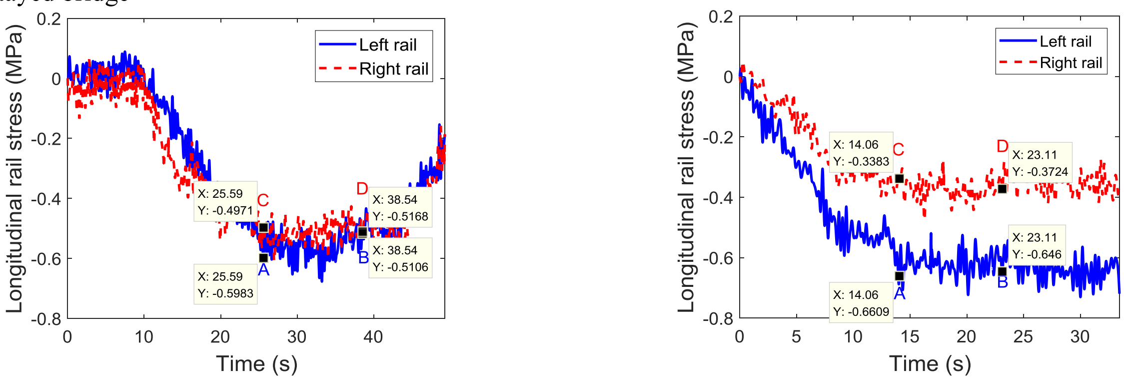

(a) first time

(b) second time

Fig. 8 Measured longitudinal rail stresses at left girder end when one train accelerated at the middle of the cable-stayed bridge

Table 3 Comparison of longitudinal additional rail stresses at left girder end between field test and finite element result

| $\Delta T$ (°C ) | Additional bending stress when two trains met at the middle of the mid-span (MPa) | | | Additional rail stress when one train accelerated at the middle of the side-span (MPa) | | | Additional rail stress when one train accelerated at the middle of the mid-span (MPa) | | |
|---|---|---|---|---|---|---|---|---|---|
| | Field test | FE result | Relative deviation* | Field test | FE result: Accelerating | FE result: Bending⊕ accelerating* | Field test | FE result: Accelerating | FE result: Bending⊕ accelerating |
| -3.75 | -11.17 | -16.53 | 47.9% | Less than 2.80 | 1.18 | 2.13 | Less than -0.52 | -0.56 | -5.75 |
| 0 | | -16.56 | 48.2% | | 1.19 | 2.14 | | -0.56 | -5.74 |
| 6.25 | | -7.92 | -29.1% | | 1.20 | 2.15 | | -0.35 | -2.83 |

*Relative deviation = (FE results-Field test results)/Field test results; ⊕: The more realistic combination of loading cases, which takes loading history into account

Figs. 7 and 8 depict respectively the measured time-histories of the longitudinal rail stresses for the latter two traction cases with the marks A, B, C, and D for the maximum additional traction stresses. Zeroing errors have already been eliminated in the data processing for Fig. 8. It can be seen from Figs. 7 and 8 that the measured stresses in the two parallel rails match well with each other. This justifies the accuracy of the test results to some extent.

The measured additional traction stresses of the rails are also listed in Table 3, by using the mean value of the maximum rail stresses of the two rails under two repeated tests for each loading cases. Nonetheless, since the vehicle locations at which the additional traction stresses reached maximum (accelerating from the middle of the side/main span) were not the same with that at the starting time of the measurement, meaning that the additional bending stresses were also different. Therefore, the actual additional traction stress should be less than the measured value for that the latter contained a portion of the additional bending stress.

### 3.2 TBI model and analysis

A TBI model was developed for this cable-stayed bridge employing the friction-spring model. Some mechanical parameters of the bridges were estimated first and later updated by the measured frequencies of the bridge.

Fig. 9 shows a planar schematic model of the cable-stayed bridge together with a seven-span simply supported U-shaped elevated bridge on each side. The rail above the bridge was set to be 250 m longer than the bridge on each end to account for the truncation of the elevated bridge. A RED was simulated at the middle of the cable-stayed bridge by disconnecting the rail.

Table 4 lists the primary geometry and material parameters of the TBI system. The CHN60 rail section was used in this model, and a 6 mm vertical wear was considered in the calculation of the dynamic bending stress in the rail (TB 10015-2012 2012). The height of the girder at the pylon was designed to be 5.6 m (Section 1 in Table 4 and Fig. 9); uniform height of 3.0 m was designated for the girder at the middle and side spans (Section 3); tapered sections following parabolic curve were designed for the rest of the girder segments connecting these two parts. To simplify the FE model, these tapered sections were uniformly represented by the section located at one third (near pylon) of the total length of the variable section segment (Section 2). High performance concrete was used for the main girder. Two different sections were considered respectively for the anchoring and the general cables. The pylon's vertical distribution along the longitudinal plane followed a curve (see Fig. 5(b)), and tapered sections were used to simulate its actual stiffness.

The TBI system was discretized in the commercial software ABAQUS by 3380 beam elements for the girders and pylons, 40 truss elements for the cables, 2261 friction spring elements, and 2049 linear spring elements representing the WJ-2 fasteners and piers. The girder nodes were set on the upper surface of the deck where the fasteners were installed and eccentric distances were input into the section information (see Fig. 9). Rigid-beam elements were applied to consider the height differences of the girder and the bearings in the vertical direction. The girder and the tower shared a node at their intersection. The detailed boundary conditions were also illustrated in Fig. 9.

The friction-spring model was included in the loading-history-based TBI static analysis for various load cases following the subsequent steps: (1) activate the linear springs and friction springs I with maximum friction force $F_u$ at the initial stage, and calculate the responses of the TBI system under the seasonal temperature change of the whole system($\Delta T$); (2) calculate the responses of the TBI system under the daily temperature variation of the rail relative to the bridge ($\Delta T_{rb}$), considering the nonlinear superposition effect of previous responses; (3) activate the friction springs II with the maximum friction force of ($F_l$-$F_u$) and then account for the TBI responses due to the vertical trainload ($W$); and (4) finally calculate the effect of the traction/braking of the train ($P$).

The FE model of the bridge can be established complying with the design documents. However, due to the uncertainty in the interaction between soil and the pier-foundation system, the longitudinal stiffness of the substructure could not be easily calculated with high degree of accuracy. Cutillas (2008) found out that the soil structure stiffness had a relevant importance in the TBI responses induced by train braking, and larger responses were obtained by taking into account the flexibility of the soil-foundation structure. Thus, its effect was considered by updating the longitudinal stiffness at pier-top with rigid foundation using test results.

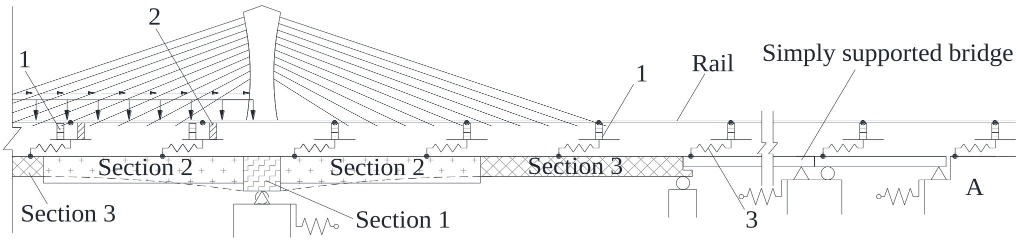


1. Friction spring I modelling the maximum static friction without vertical load; 2. Friction spring II modelling the increase in the maximum static friction induced by vertical load; 3. Linear spring modelling the stiffness of the fastener; A. Embankment

Fig. 9 Schematic planar model for the proposed TBI model allowing for loading-history effects

Table 4 Primary geometry and material parameters of the TBI system

| | |
|---|---|
| Standard span of the simply supported bridge | $L_s = 30$ m |
| Length of the cable-stayed bridge | $L_c = 80+140+80 = 300$ m |
| Updated elastic module of the simply supported bridge | $E_s = 4.62\times10^{10}$ N/m$^2$ |
| Updated elastic module of the main girder of the cable-stayed bridge | $E_{cg} = 5.04\times10^{10}$ N/m$^2$ |
| Updated elastic module of the pylon of the cable-stayed bridge | $E_{cp} = 4.83\times10^{10}$ N/m$^2$ |
| Stiffness of the elastic support for the simply supported bridge (two lines) | $k_s = 6.629\times10^7$ N/m |
| Stiffness of the elastic support at right main pier of the cable-stayed bridge | $k_c = 1.368\times10^9$ N/m |
| Area of the worn 60 kg/m rail in China | $F = 7.745\times10^{-3}$ m$^2$ |
| Moment of inertia for the worn 60 kg/m rail in China | $I_x = 2.879\times10^{-5}$ m$^4$ |
| Area of the main girder of the cable-stayed bridge (Section 1) | $F_{c1} = 4.354\times10$ m$^2$ |
| Moment of inertia for the main girder of the cable-stayed bridge (Section 1) | $I_{xc1} = 1.147\times10^2$ m$^4$ |
| Area of the main girder of the cable-stayed bridge (Section 2) | $F_{c2} = 1.331\times10$ m$^2$ |
| Moment of inertia for the main girder of the cable-stayed bridge (Section 2) | $I_{xc2} = 3.216\times10$ m$^4$ |
| Area of the main girder of the cable-stayed bridge (Section 3) | $F_{c3} = 9.724$ m$^2$ |
| Moment of inertia for the main girder of the cable-stayed bridge (Section 3) | $I_{xc3} = 1.264\times10$ m$^4$ |
| Area of the girder of the simply supported bridge (two lines) | $F_s = 4.48\times10^0$ m$^2$ |
| Moment of inertia for the girder of the simply supported bridge (two lines) | $I_s = 1.72\times10^0$ m$^4$ |
| Area of the cable section (inside) | $F_{ci} = 5.32\times10^{-3}$ m$^2$ |
| Area of the cable section (anchored in the end) | $F_{ce} = 7.56\times10^{-3}$ m$^2$ |

According to engineering experience, the actual strength of the concrete is always larger than its design value because the latter has the guarantee rate of 95%. Therefore, the elastic module of the concrete was increased by 30% relative to the design value, while the longitudinal stiffness at pier-top ($k_s$) considering foundation flexibility was adjusted to 0.78 times that with rigid foundation so that the natural frequencies of the FE results ($f_l$ = 1.77 Hz, $f_v$ = 4.60 Hz) matched the test results within a 1.6% difference. The 30% increase in the elastic module of the concrete was based on the field test results for a simply-supported concrete bridge of this metro line.

For the cable-stayed bridge, the pier model with stiffness matrix in the bottom representing the flexibility of the soil-foundation structure was established. The longitudinal stiffness at main pier-top was then calculated and input into the modal analysis model for the cable-stayed bridge. The elastic module of the concrete was increased by 40% compared with its design value, and the longitudinal stiffness at main pier-top ($k_c$) was adjusted to 0.14 times that in the case of rigid foundation. As a result, the differences of the first three natural frequencies of the cable-stayed bridge obtained via field test and the updated FE model were all within 5.2%, as were listed in Table 2. Modal shapes were not identified in the field tests for both structures and was predicted solely by FE models.

To allow for the actual condition, multiple cycles of passing trains occurring after seasonal temperature change (Widarda 2008), which would significantly change the longitudinal resistances of the fasteners and rail stresses, should be performed before the simulation of the daily temperature change and the test loading case. Ruge *et al.* (2009) included such effect in their analysis, and considerable increase was observed in the linear elastic parts along the track–bridge coupling interface.

Another attempt to match the measurements with theoretical results as close as possible was to measure all the data when the rail temperature had attained the fixing temperature of the rail, and it was assumed that at that moment the rail was stress-free (Fryba 1996).

Lacking the time-history temperature data and the actual fixing temperature of the rail, a reasonable range was given to simulate the actual behavior as close as possible. According to the Chinese CWR code (2012), the design stress-free temperature of the rail in Shanghai is recommended to be (24.75±5) °C. Since the tests were performed on a summer night with the atmospheric temperature of 26 °C, the rail temperature was assumed to be the same with the ambient temperature because of the good thermal conductivity of the steel, so the seasonal temperature change $\Delta T$ should be between -3.75 °C and 6.25 °C. The rail stresses under the initial conditions of $\Delta T$=-3.75 °C, $\Delta T$=0 °C and $\Delta T$=6.25 °C were respectively calculated in the following section. And the daily temperature difference $\Delta T_{rb}$ was considered to be 0 °C at

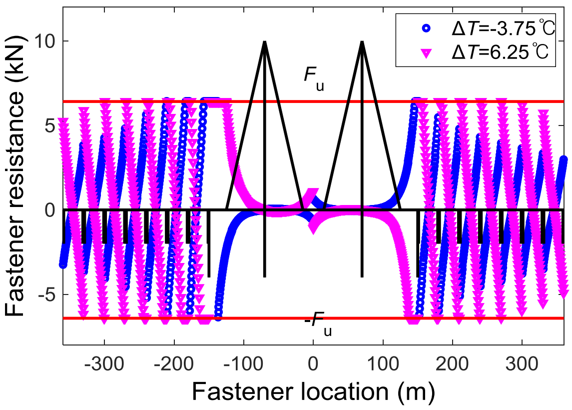


(a) fastener resistance forces induced by $\Delta T$

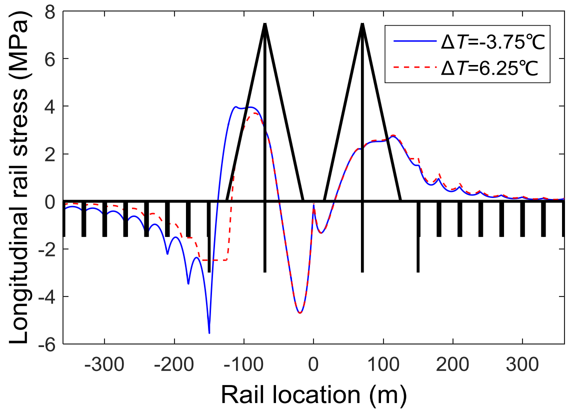


(b) additional rail stresses due to bending

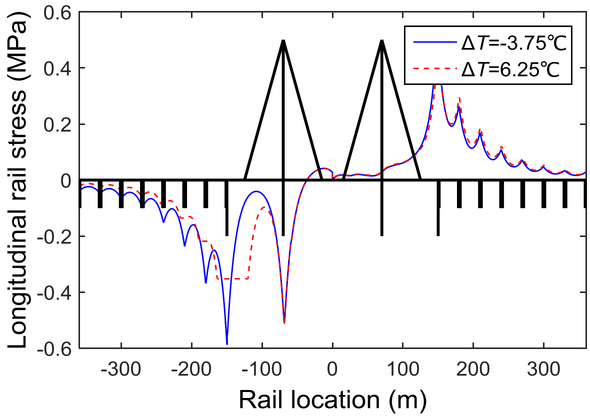


(c) additional rail stresses due to traction

Fig. 10 Distribution of fastener resistance forces and additional rail stresses when the train left from $S_2$

midnight. Equivalent line loads distributed along the 68.4-m train length were used to simulate the vertical trainload ($w$=28070 N/m for each train) and the longitudinal traction rate was set to be 0.1 according to the acceleration of the train during departure.

### *3.3 Comparison and discussion*

Table 3 shows the longitudinal additional rail stresses at the left girder end obtained from the above loading-history-based TBI model together with the measured ones. The measured maximum longitudinal rail stress at left girder end when one train accelerated at the middle of the mid-span (-0.52 MPa) should contain the additional traction stress and a portion of additional bending stress, the same is true with the maximum measured data when one train accelerated at the middle of the side-span (2.80 MPa). These measured stresses are in accordance with the FE results, as the former (-0.52 MPa) is within the range from -0.35 MPa to -5.75 MPa, while the latter (2.80 MPa) is quite close to the calculated range of 1.18 MPa to 2.15 MPa. Moreover, the measured maximum additional bending rail stresses when two trains met at the middle of the mid-span (-11.17 MPa) was within the range from -7.92 MPa to -16.56 MPa, as calculated by TBI analysis. The overall agreement between the measured and computed results indicates that both the updated TBI model and the proposed friction-spring model are reliable.

The differences between the measured and computed additional bending rail stresses when two trains met at the middle of the mid-span were in the range from -29.1% to 48.2%. This non-negligible difference shows the difficulty in the validation of numerical models through field tests. It is noted that possible errors might exist in the measurement of such small rail stresses, thus leading to difference between field test and FE results. In addition, this phenomenon might be explained by the consideration of load history in this study as follows.

First, the initial thermal variation could cause obvious difference in the distributions of fastener plasticity (as illustrated in Fig. 10(a)), so the temperature effect could significantly influence the rail stress under vertical train load (as demonstrated in Table 3). However, the complicated temperature field under sunshine in the bridge structure, especially for concrete box girder, made the precise measurement of additional rail stress solely induced by thermal variation almost impossible (Elbadry and Ghali 1983). Higher level of accuracy in TBI analysis could be achieved if more accurate temperature variations can be obtained. Second, the unpredictable residual stresses due to the repeated temperature changing and passing trains could also lead to difference between the actual structure and the FE simulation.

The distribution of longitudinal additional rail stresses due to bending and braking are illustrated in Figs. 10(b) and (c) respectively. It can be indicated that the measuring point of longitudinal rail stress at left girder end represents the most critical position of the additional compressive stresses due to bending and traction forces. Both Table 3 and Fig. 10 show that the additional traction stresses are quite small for this bridge, and won't be a governing factor for the strength of the rails; on the other hand, the additional bending stresses are much larger than those induced by traction. Both scenarios contradict with the findings for the simply supported bridge (Zhang *et al.* 2015). This is because the pier stiffness of the cable-stayed bridge is much larger than that of simply supported bridges, while the vertical stiffness of the bridge structure is significantly smaller. In addition, the longitudinal force of the test train with three cars is not big enough to cause large movement of the bridge in the girder ends.

Though the vertical trainload and braking/traction forces are time-varying in nature, only the constant static train loadings acted at fixed position were considered in the current TBI analysis framework. To allow for feasible comparison between the maximum rail stresses acquired in the field test and those of the TBI analysis, the vertical and longitudinal vehicle-induced loads should be exerted at the most unfavorable locations based on the judgment of structural behaviors. In a more realistic TBI analysis, the vertical trainload and longitudinal braking force should be considered as moving loads so as to get a full envelope of the longitudinal rail stress, and the resistance of each fastener should be changed instantly according to the its relative position with the moving trainload.

## 4. Conclusions

A series of laboratory tests have been performed on the longitudinal resistance properties of three types of rail fasteners commonly used in urban rail transit traffic in China. A friction-spring model has been proposed to convey explicit physical behavior of the fasteners, and to include the loading-history effects and changes in longitudinal resistance of the rail fasteners in various load cases. The proposed resistance model was then applied in a TBI system for a cable-stayed bridge. The longitudinal stiffness of the piers and the vertical stiffness of the bridges were updated according to field test results. And the TBI model was verified through the comparison of calculated and measured rail stresses under moving trains. The updated and validated model can be employed to figure out the necessity of RED and the effect of the calculation methods in the future.

Currently, the friction-spring model could only apply to the urban rail transit fasteners tested in this study, unless more relevant studies were to be performed to verify its applicability to other types of fasteners. The limitation of the study lies in the ignored dynamic and time-varying effect of the moving trains and the changes of fastener resistance with the moving of the wheel loads. More realistic TBI analysis model allowing for these factors remains to be established.

## Acknowledgments

The authors are grateful for the financial support received from the National Natural Science Foundation of China (No. 51278374) and the Project Funded by the Priority Academic Program Development of Jiangsu Higher Education Institutions.

## References

Bin, Y., Dai, G.L. and Zhang, H.P. (2012), "Beam-track interaction of high-speed railway bridge with ballast track", *J. Central South U Technol. (English Ed.)*, **19**(5), 1447-1453. https://doi.org/10.1007/s11771-012-1161-8.

Chen, R., Wang, P. and Wei, X.K. (2013), "Track-bridge longitudinal interaction of continuous welded rails on arch bridge", *Math. Problems Eng.* **2013**. http://dx.doi.org/10.1155/2013/494137.

Cutillas, A.M. (2008), "Track-bridge interaction problems in bridge design", *Track-Bridge Interaction on High-Speed Railways*, 19-28.

Dai, G. and Yan, B. (2012), "Longitudinal forces of continuously welded track on high-speed railway cable-stayed bridge considering impact of adjacent bridges", *J. Central South U*, **19**(8), 2348-2353. https://doi.org/10.1007/s11771-012-1281-1.

Dai, G.L. and Liu, W.S. (2013), "Applicability of small resistance fastener on long-span continuous bridges of high-speed railway", *J. Central South U*, **20**(5), 1426-1433. https://doi.org/10.1007/s11771-013-1631-7.

De Backer, H., Mys, J. and Van Puymbroeck, E. (2017), "Influence of temporary bridge decks on continuously welded rails", *Ce/papers*, **1**(2-3), 1335-1343. https://doi.org/10.1002/cepa.175.

Deladi, E.L. (2006), *Static Friction in Rubber-Metal Contacts with Application to Rubber Pad Forming Processes*. University of Twente, Enschede, the Netherlands.

DIN-Fachbericht 101 (2003), *Lasten und Einwirkungen auf Brücken einschließlich Kombinationsregeln*. Berlin, Germany.

Elbadry, M. M. and Ghali, A. (1983), "Temperature variations in concrete bridges", *J. Struct. Eng.*, **109**(109), 2355-2374.

EN 1991-2 (2003), *Eurocode 1: Actions on structures. Traffic loads on bridges (Part 2)*. Belgium.

Esveld, C. (1995), "Avoidance of expansion joints in high-speed CWR track on long bridges", *Rail Eng. International Ed.*, 7-9.

Esveld, C. (1998), "Improved knowledge of CWR track", *Interactive Conference on Cost Effectiveness and Safety Aspect of Railway Track*, Paris, France.

Esveld, C. (2001), *Modern Railway Track*, Zaltbommel, MRT Production, Netherlands.

Fryba, L. (1996), *Dynamics of Railway Bridges*, Thomas Telford Publishing, London.

GB 50157-2013 (2014), *Code for Design of Metro*. Beijing, China.

Gimsing, N.J. and Georgakis, C.T. (2011), *Cable supported bridges: Concept and design*, John Wiley & Sons, USA.

Hu, N., Dai, G.L., Yan, B. and Liu, K. (2014), "Recent development of design and construction of medium and long span high-speed railway bridges in China", *Engineering Structures*. Elsevier Ltd, **74**, 233-241. https://doi.org/10.1016/j.engstruct.2014.05.052.

IAPF (2007), *Instrucción de acciones a considerar en el proyecto de puentes de ferrocarril, Ministerio de Fomento de España*. Madrid, Spain.

Lim, N.H., Park, N.H. and Kang, Y.J. (2003), "Stability of continuous welded rail track", *Comput. Struct.*, **81**(22-23), 2219-2236.

Liu, W.S., Dai, G.L. and He, X.H. (2013), "Sensitive factors research for track-bridge interaction of Long-span X-style steel-box arch bridge on high-speed railway", *J. Central South U*, **20**(11), 3314-3323. https://doi.org/10.1007/s11771-013-1855-6.

Mirza, O., Kaewunruen, S., Dinh, C. and Pervanic, E. (2016), "Numerical investigation into thermal load responses of railway transom bridge", *Eng. Failure Analysis*, Elsevier Inc., **60**, 280-295. https://doi.org/10.1016/j.engfailanal.2015.11.054.

Okelo, R. and Olabimtan, A. (2011), "Nonlinear Rail-Structure Interaction Analysis of an Elevated Skewed Steel Guideway", *J. Bridge Eng.*, **16**(3), 392-399.

Roth, F.L., Driscoll, R.L. and Holt, W.L. (1943), "Frictional properties of rubber", *Rubber Chem. Technol.*, **16**(1), 155-177. https://doi.org/10.5254/1.3540095.

Ruge, P. and Birk, C. (2007), "Longitudinal forces in continuously welded rails on bridgedecks due to nonlinear track-bridge interaction", *Comput. Struct.*, **85**(7-8), 458-475. https://doi.org/10.1016/j.compstruc.2006.09.008.

Ruge, P., Widarda, D.R., Schmälzlin, G. and Bagayoko, L. (2009), "Longitudinal track-bridge interaction due to sudden change of coupling interface", *Comput. Struct.*, Elsevier Ltd, **87**(1-2), 47-58. https://doi.org/10.1016/j.compstruc.2008.08.012.

Ryjáček, P. and Vokáč, M. (2014), "Long-term monitoring of steel railway bridge interaction with continuous welded rail", **99**, 176-186. https://doi.org/10.1016/j.jcsr.2014.04.009.

Ryjáček, P. *et al.* (2016), "The Rail-bridge Interaction - Recent advances with ERS fastening system for steel bridges", *Transportation Research Procedia*, **14**, 3972-3981. https://doi.org/10.1016/j.trpro.2016.05.494.

Smith, R.H. (2008), *Analyzing Friction in the Design of Rubber Products and Their Paired Surfaces*, CRC press, Florida, USA.

TB 10015-2012 (2012), *Code for Design of Railway Continuous Welded Rail*, Beijing, China.

TB 10621-2009 (2009), *Code for Design of High Speed Railway*, Beijing, China.

UIC 774-3R (2001), *Track/bridge Interaction: Recommendations for Calculations*. Paris, France.

Wang, P., Zhao, W., Chen, R. and Xiao, J. (2013), "Bridge-rail interaction for continuous welded rail on cable-stayed bridge due to temperature change", **16**(8), 1347-1354. https://doi.org/10.1260/1369-4332.16.8.1347.

Wenner, M., Lippert, P., Plica, S. and Marx, S (2016), "Track-bridge-interaction - Part 1: historical development and model", *BAUTECHNIK*, **93**(2), 59-66.

Widarda, D.R. (2008), *Longitudinal forces in Continuously Welded Rails due to Nonlinear Track-Bridge Interaction for Loading Sequences*, Technische Universität Dresden,

Yang, S.C. and Jang, S.Y. (2016), "Track-bridge interaction analysis using interface elements adaptive to various loading cases", *J. Bridge Eng.*, **21**(9), 4016056.

Zhang, J., Wu, D.J. and Li, Q. (2015), "Loading-history-based track-bridge interaction analysis with experimental fastener resistance", *Eng. Struct.*, **83**, 62-73. https://doi.org/10.1016/j.engstruct.2014.11.002.

*PL*